2016-12

Semiautomatic friction stir welding of 38 mm OD 6082-T6 aluminium tubes

Hattingh, DG

10.1016/j.jmatprotec.2016.07.027
JOURNAL OF MATERIALS PROCESSING TECHNOLOGY
Elsevier BV

Friction Stir Welding of 38 mm OD 6082-T6 Aluminium Tubes – Process Development and Microstructure

D. G. Hattingh[1] , L. G. von Welligh[1] , D. Bernard[1], L. Susmel[2] , R. Tovo[3], and M. N. James[1, 4]

[1] Department of Mechanical Engineering, Nelson Mandela Metropolitan University, Port Elizabeth (South Africa)
[2] Department of Civil & Structural Engineering, University of Sheffield, Sheffield (UK)
[3] Department of Engineering, University of Ferrara, Ferrara (Italy)
[4] School of Marine Science & Engineering, University of Plymouth, Plymouth (UK)
e-mail: danie.hattingh@nmmu.ac.za; mjames@plymouth.ac.uk

Keywords: Friction stir welding; 6082 aluminium alloy; small diameter tube; electron back-scatter diffraction; retracting pin tool

Abstract

This paper describes the development of a semi-automated friction stir welding (FSW) technique for joining 38 mm nominal outer diameter (OD) tubes of 6082-T6 aluminium alloy with 3.5 mm nominal wall thickness. Process development for this application of FSW required the integration of a rotational axis with the control system of the FSW machine as well as the development of a secondary human-machine interface (HMI) for this axis and also necessitated the design of a retracting tool pin in order to eliminate the exit hole of the pin. Issues relating to tube support, variation in wall thickness and out-of-roundness during welding are not straightforward for thin tube. The main topics covered in this paper are FSW process design and optimisation together with a discussion of the resulting weld zone microstructure. This welding work underpinned a substantial international network project whose aim was to prove the viability of FSW for making high performance joints in extruded aluminium tubes of diameter suitable for fabricating structural components, e.g. for ground vehicles, and to systematically investigate the fatigue performance, fracture paths, associated microstructural changes and mechanical properties under the type of multiaxial loading (biaxial tension-torsion) that tubes might experience in service.

Introduction

Friction stir (FS) welding is a highly successful solid-state joining process that offers high levels of joint performance with low requirements for preparation and post-weld dressing. The high levels of plastic work induced in the weld zone produce a very fine recrystallized grain size in the stirred region of the weld (i.e. in the weld nugget), whilst the low heat input limits residual stresses to a relatively low fraction of the proof strength of the weld metal, at least in the direction transverse to the weld, which is usually important in fatigue crack initiation, e.g. James et al. (2004) using synchrotron X-ray diffraction reported peak tensile values of < 30 MPa for the transverse residual stresses in FSW of 8 mm plate of 5383 aluminium alloy. These effects are generally beneficial to weld dynamic

performance. Alongside these advantages, the process can be used to join dissimilar metals and alloys that may be difficult to fusion weld, e.g. Wu et al. (2013) have reported work using FSW to join 2 mm plates of Ti-6Al-4V to 6061-T6 aluminium alloy, while Kamp et al. (2007) presented a combined modelling approach (thermal, microstructural and strength) of the FSW process for 400 mm thick plates of 7449 aluminium alloy and of 6.5 mm thick plates of 7150 aluminium alloy. There has therefore been a substantial take-up of FSW in structural fabrication across a wide range of industrial sectors; Shah and Tosunoglu (2012), for example, have presented a review of the current state of the art in FSW and their view of its prospects for the future across a wide range of application sectors. A number of workers have considered FSW applications in such areas as ship building (Colligan 2004), transportation (Thomas and Nicholas 1997), and aircraft Burford et al. (2006). In the case of the aircraft industry the industrial use of FSW is now so widespread that both the American Welding Society and NASA have published technical standards for friction stir welding of aerospace hardware fabricated from aluminium alloys (American Welding Society, 2010; NASA, 2012).

Tubular space-frame structures are widely used in ground vehicle chassis design, and deploying FSW techniques in joining of tubes has particular challenges in terms of the criticality of pin plunge depth in thin-walled tube and support for the material during welding, and also in terms of arranging tool pin retraction as a weld is completed, in order to avoid the typical exit pin hole in the joint line as this would constitute a substantial defect in thin-walled tube. This paper describes the development of a friction stir welding process for joining extruded 6082-T6 aluminium alloy tubes with nominal outer diameter (OD) of 38 mm and a wall thickness of approximately 3.5 mm (giving a nominal inner diameter (ID) of some 31 mm) that solves these issues and gives high quality, repeatable welds.

An MTS I-STIR™ Process Development System provided the foundation for this project, which required coupling tube rotation via a worm gear motor drive with a tube support system and integrating the drive system control with tool control of the I-STIR platform. Figure 1 shows these components mounted on the work table of the I-STIR process development platform.

This is one of very first applications of FSW to small diameter tubular geometries to be reported in the open literature. Peterson et al. (2011) filed a US patent application in 2011 for a process to friction stir weld casings and small diameter tubing or pipe, although they defined ‘small’ diameter as an ID ≈ 228 mm. Lammlein et al. (2012) have published work dealing with the development of a process for FSW of 6061-T6 aluminium tubes 107 mm in diameter and with a wall thickness of approximately 5.8 mm. Both of these cases deal with substantially larger diameters than the 38 mm tube used in the present work and this smaller size was chosen to be representative of the dimensions that might be used in space frame chassis design for ground vehicles. Chen et al. (2015) recently published work describing a FSW process for joining 19 mm diameter pipes of 3003 aluminium alloy 1.5 mm thick to pure copper with a 1 mm wall thickness. The application of FSW to

repair of small diameter (25 mm to 100 mm) coiled tubing (CT) has been discussed by Steel et al. (2013). Coiled tubing is widely used in the oil and gas industry and its repair together with the associated downtime of the plant has a high cost. Steel et al. (2013) state that FSW gives a repair joint with near-base metal mechanical and fatigue properties. These authors further note that tool design becomes critical along with design of an internal supporting mandrel that can be removed after welding. The weld is a critical part of the tube and a reduction in thickness across the joint is not tolerated in the finished product. A consumable ring is therefore used that has a profile that is "proud" relative to the outside diameter of the tube. This allows for a finished joint having an excess thickness in the joint area. This can then be ground back to the tube diameter after welding. Doos and Abdul Wahab (2012) have reported some limited work on friction stir welding of small (but unstated) diameter 6061-T6 aluminium tube using a modified milling machine. Their process used an internal mandrel to support the tubes but apparently did not include any tool retraction to remove the exit hole defect. They appear to have reported tensile results obtained from sections cut from the welded tubes rather than complete tube data. Some of their weld sections achieved a maximum tensile strength of 62% of the parent plate, but their data was very scattered and defects were common in their welds.

Tool design in tube welding is critical and, as noted above, it is important in FSW of small diameter tubes, where provision for run-on and run-off tabs cannot be provided, not to leave any hole in the joint line after extracting the tool at the end of the welding process. Any residual plunge hole in the joint would act as a very significant weld defect, given the relative sizes of the tool pin, tube diameter and tube wall thickness. A tool with a retractable pin was therefore designed and developed for this particular FSW application.

Development of the FSW Process

In developing a robust and reliable FSW process for manufacturing the circa 100 tube specimens required for the multiaxial fatigue testing programme, with confidence that their properties would be consistent enough to draw valid performance conclusions, a number of individual tasks had to be accomplished. These included:

- Designing and building the worm gear drive and clamping system for welding
- Electronic integration of the tube rotational axis and control system into the control software of the I-STIR process development system and development of a suitable HMI.
- Designing and validating the retractable pin tool used in the welding process
- Determination of suitable welding process parameters to achieve the required weld quality
- Production of an initial set of ~200 mm long welded test specimens for microstructural and mechanical property characterisation of the joint

Tube support and clamping system

The tube welding system is shown schematically in Figure 2 and consists of three main components, the helical worm gear motor that rotates the tube (A), the tube-to-motor coupling (B) and the tube bearing support and clamping system (C). Figure 3a shows two tube sections ready for welding mounted in the support and clamping system, while Figure 3b shows an equivalent cross-sectional view that gives details of the bearing support and integrated clamping system. The various components in Figure 3 are identified as:

1. Precision locknut
2. Fenlock cone clamp
3. Flange connecting motor to tube drive shaft
4. Support bearings
5. Mandrel drive bolt
6. Internal tube support mandrel

Tube sample clamping was achieved by sliding the two tubes to be welded onto the supporting mandrel (6) and securing them with precision lock nuts (1). This sub-assembly was coupled to the flange on the worm gear drive using a drive bolt (5) and then positioned within the bearing supports (4) by means of Fenlock cone clamps (2). The process of aligning the tubes and clamping them in position for welding is quite time-consuming and any extension of this process into industry would require an increased level of automation to be introduced into the process. Key issues in the set-up and clamping process which are fundamental to achieving a high quality weld include achieving good joint fit-up, accurate tube-to-tube alignment and adequate contact between the tube and backing (the tube drive shaft). The heat retention makes it increasingly difficult to release the cone clamps (probably because of expansion of the threads on the release bolts which led to replacement of a number of these bolts during the production run of circa 100 specimens). The 6082-T6 aluminium was supplied as 3 m long tubes with nominal dimensions of 38 mm nominal OD and 31 nominal ID, giving approximately 3.5 mm wall thickness. Tube-to-tube alignment and achieving a consistent quality of welding were complicated both by an observed variation in wall thickness of the tube of up to 0.3–0.5 mm, which created eccentricity in the tubes. In addition a degree of tube ovality was also observed. It was therefore found necessary to machine the tube OD to 37.5 mm to improve tube alignment during set-up, giving a final tube thickness of approximately 3.0 mm ± 0.1 mm. More critically it allowed the use of a simplified weld control strategy in which the pin length could be fixed throughout the weld run without introducing root flaws due to insufficient pin penetration.

Retractable pin tool

The MTS I-STIR processing platform has in-built capability of hydraulically retracting a tool pin that is screwed into its tool head. Movement of the tool pin is therefore possible independently of the z-

axis movement of the tool spindle. A two-piece tool was therefore designed to allow tool retraction to occur at the end of the welding process and the components are illustrated in Figure 4, while a typical pin assembly is shown in Figure 5. Both components were manufactured from X40CrMoV5-1 hot work tool steel to DIN 1.2344, vacuum heat treated and double tempered to a Rockwell hardness value of HR_C 54. The tool has a concave shoulder with a 6° angle.

After external machining to an OD of 37.5 mm, the pin length corresponding with a nominal pin penetration depth of 85% of the remaining wall thickness was calculated as 2.45 mm (taking account of tool tilt and of tube thickness variation). The shoulder pitch angle was 2° and, in order to achieve the correct pin penetration depth, it is important to locate the tool exactly at the tube centreline prior to commencing the welding process. Any lateral displacement of the pin will lead to problems with weld shoulder undercut and weld ligament variation (this ligament is the amount of material at the root of the weld that is not directly stirred by the pin, and is the favoured location of FSW root defects, also known as 'kissing bonds'. These bonds and their influence have been described by Dickerson and Przydatek (2003) for 5083-O, 5083-H321 and 6082-T6 aluminium alloys, while James et al. (2005) considered the complete range of defects, including 'kissing bonds' found in friction stir welded butt joints in 5083-H321 alloy. In the present work, pin penetration was verified by considering weld cross-sections from initial test welds.

The weld is made using position control with the tool pin locked in position at the correct penetration depth and a total plunge depth of 2.5 mm (which ensures adequate shoulder contact). Thus during the majority of the welding process, the pin acts like a fixed pin tool. After 630° of rotation the pin is hydraulically retracted at a steady rate over a further quarter revolution (90° of rotation) with the tool shoulder kept in the plunge position. Thus the total weld sequence occurs over two complete revolutions of the tube (720°). Only once the tool pin is completely retracted is the shoulder lifted from the tube surface and tool rotation stopped. Pin retraction rate was also optimised on the basis of metallographic examination to determine the conditions that led to a sound weld retraction region. Tunnel defects were found to occur when the retraction rate was too high.

Human-machine interface (HMI)

The HMI developed for this work has two modes of operation, a default start-up manual mode that allows the user to start and stop the machine at will, and an automatic mode where the user can specify an rpm activation value at which the welding process will stop and start. The process can be stopped at any time by pressing the abort button. The automatic HMI is illustrated in Figure 6 and the following inputs are available to the user in the various zones indicated in the figure:

Zone 2.1: The "MODE" option allows the user to select the appropriate control mode, either automatic or manual mode. The "UNITS" option allows the user to specify the tube rotational speed either as the shaft rpm of the motor or as mm/min.

Zone 2.2 MTS Platform: When the system is in manual mode, there are no configurable options for the MTS I-STIR platform; in automatic mode, two options are available:

Auto-detect mode – This is disabled by default. The user must enable this option before it is possible to modify the activation value of tool rpm where welding commences.

Activation value (tool rpm) - This activation value is the rpm value of the MTS spindle at which the system will activate.

Zone 2.3 Motor: The "INPUT" box allows the user to set the welding parameters. The left hand boxes are input values and the right hand boxes show the current active values. The user must click the "Apply" button to apply the new settings. The customizable parameters are "Shaft rpm" that sets the rpm of the output shaft of the tube drive motor. If the system is in set to mm/min, this value can be entered as a feed rate in mm/min instead of as an rpm value. "Ramp" refers to the acceleration value. The unit of this value correlates to the current system configuration. "Pipe Diameter" allows the user to enter the outside diameter (OD) of the pipe to be welded, which is necessary in order to use the mm/min feed rate input option.

Zone 2.4 Help Menu: The "Help" menu provides options to obtain assistance with a variety of settings, including the I-STIR rpm activation values and the various input data that must be set on the I-STIR platform.

Welding process parameters

A number of welding parameter combinations were tried before settling on a final set that gave welds with acceptable surface quality, low defect level and high tensile strength. Attention was first given to achieving a weld surface finish suitable for components subject to fatigue loading. The main parameters evaluated were plunge rate, feed rate and spindle rotational speed. Figure 7 and its associated Table 1 demonstrate the influence of a number of weld process parameters on weld surface appearance. Weld surface finish was further optimised by maintaining shoulder contact with the tube surface through two complete revolutions (720°); the first pass improves the uniformity of shoulder contact and the second pass then improves the surface finish. The diameter of the tool shoulder was originally 12 mm, but the surface contact area on the tubes was found to be too small with a shoulder plunge depth of 0.1 mm. A reduction in tool shoulder diameter to 10 mm produced a better surface finish. The final parameters used to join the fatigue specimens included using a tool with a shoulder diameter of 10 mm rotating at 600 rpm, a rotational tube feed rate of 50 mm/min, and a tool pitch angle of 2°, with a total plunge depth of 2.5 mm and a pin length of 2.45 mm.

The welding process then follows the following sequence of events:

1. Pin moves toward weld centreline
2. Pin touches tube for zero reference of plunge depth
3. Start spindle rotation
4. Plunge pin and shoulder to correct depth

5. Ensure shoulder in good contact with pipe
6. Initiate pipe rotation
7. Rotate pipe 720° to achieve good surface finish (2 full revolutions)
8. Initiate pin retraction after 630° rotation keeping pipe rotating to eliminate exit hole
9. Retract shoulder (only once the pin is fully retracted)

It is important to note that even once a set of process parameters has been identified that leads to sound welds, relatively small variations in either tube eccentricity or ovality and/or a pin misalignment with respect to the weld centreline, can lead to the presence of weld defects. Figure 8 shows a typical defect observed in a production weld when the pin is slightly misaligned.

Mechanical Properties

The tensile properties of a welded joint are a reasonable first order indicator of the joint quality and hence 'joint efficiency' (defined as the ratio of tensile strength of the weld to that of the parent plate) is often used to describe the mechanical performance of welded joints. In the present case the tensile strength was measured on complete tube specimens and also on microtensile specimens with a cross-section of 2 mm by 3 mm (Figure 9). Microtensile specimens were waterjet machined and tested on a Gatan Microtest 2000EW test module of 2 kN load capacity. The purpose of testing the microtensile specimens was to check whether any gross defects or property differences existed in the complete weld zone that might lead to significant weld-to-weld variation in mechanical properties. In fact, very consistent tensile strength values were recorded from both types of specimen, and mechanical property data in tension and in torsion are shown in Table 2. The welded joint efficiency is 0.55; this value compares well with the figure of 0.67 reported for FS welds in flat 3 mm thick plates of 6082-T6 given by Moreira et al. (2009). The microtensile specimens were polished in order to observe where failure occurred and this was found to be in the weld zone on the tool retreating side. The tube specimens failed at the tool shoulder undercut on either the advancing or retreating sides of the weld, which represent a stress concentrating feature and a reduction in load carrying area. In addition, the undercut region also experiences overaging in the heat affected zone, as can be seen in Figure 10, which shows the typical Vickers hardness variation measured across the FS weld zone at tube mid-depth under a 500 gf load, and which can be compared with the average hardness of the un-welded 6082-T6 tube (94 H_V). An image of the weld cross-section is also given in the figure at the same scale.

Microstructure

The chemical composition of the 6082 alloy is given in Table 3, and the tubes were initially in the T6 condition, i.e. solution heat treated and peak aged by dispersion hardening. FS welding of the tubes essentially anneals the alloy and reduces the strength (Table 2) and hardness (Figure 10) to values

that are close to the level found in the annealed O-condition (tensile strength about 130 MPa). The slightly higher tensile strength observed in the FS welded specimens, compared with the O-condition is a result of the strain hardening which occurs in this alloy at strain amplitude levels approximately greater than 0.82% as reported by Borrego et al. (2003). The more gradual hardness slope seen on the retreating side is attributed to the higher temperatures observed on the retreating side during welding.

Figure 11 shows a light microscope image of the microstructure of the parent plate alloy in this seamless extruded tube, using a 3D cubic representation and the grains can be seen to be slightly flattened in the through-thickness direction, as expected from an extruded product. The microstructure was revealed using Weck's solution, which contains 3g of potassium permanganate ($KMnO_4$) and 1g of sodium hydroxide (NaOH) in 100ml of water. The specimen is exposed to this solution for a few seconds and can then be viewed under polarised light. The average grain dimension and aspect ratio were for all three coordinate axis planes were determined by the intercept method and are given in Table 4 with reference to the standard longitudinal (L), transverse (T) and short transverse (S) directions with respect to the extrusion axis in the tube (indicated with the black arrow). These axes define the L-T, L-S and T-S planes which allow a standard description of the microstructure.

Once the weld process details had been optimised, a tube specimen was welded and used for further metallographic investigation of the as-welded microstructure using electron back-scatter diffraction (EBSD) in a field emission scanning electron microscope (FESEM). Several other authors have reported microstructural information for FSW aluminium alloys obtained via EBSD, but no similar work on tube specimens is available. Cho et al. (2014) considered 15 mm thick plates of extruded 5083 and 6082 aluminium alloys, in particular considering the microstructure in the fine-grained stir zones of the weld nugget. They reported a fine equiaxed grain structure in the stir zone that showed the presence of dynamic recrystallization with a strong shear texture in the 6082 alloy that was not present in the 5083 alloy.

Wang et al. (2016) reported a more detailed EBSD study of 5.85 mm thick rolled plates of FSW 6061-T6 aluminium alloy using a feed rate of 60 mm/min and two different tool rotational speeds of 600 rpm and 800 rpm. Their study should be directly comparable with the tube welds, because 6082 and 6061 are very similar aluminium alloys, while their process parameter combination of 60 mm/min and 600 rpm tool speed is close to the values used in the present study (50 mm/min and 600 rpm). Alloy 6082 has a significantly higher silicon and manganese content than 6061 that controls the grain structure and gives a higher strength alloy than 6061; 6082 has therefore replaced 6061 in many structural applications. Wang et al. (2016) did not observe any significant texture in their rolled parent plate and the weld heat-affected zone (HAZ) largely retained the grain structure

of the parent plate. In the thermomechanically-affected zone (TMAZ) they observed evidence of recovery and some dynamic recrystallisation, while in the stir zone they observed fine grains due to strain induced boundary migration and geometric dynamic recrystallisation. They note that the FSW process leads to a similar texture to that found in the extrusion process and that two partial fibre textures are induced after shear deformation in fcc metals, i.e. fibre A of the form $\{1\ 1\ 1\}\langle u\ v\ w\rangle$ and fibre B of the form $\{h\ k\ l\}\langle 1\ 1\ 0\rangle$. Texture A develops as a result of the alignment of {1 1 1} slip planes with the shear plane and texture B as the result of an alignment of the $\langle 1\ 1\ 0\rangle$ slip direction with the shear direction. In addition, a metastable texture component C can also be developed which can be denoted as $(1\ 1\ 0)[1\ \bar{1}\ 0]$. The two different tool rotational speeds that they considered led to different texture components being present in the stir zone.

Negendank et al. (2016) reported a study of the microstructural evolution of seamless 32 mm square tubes of 6060 and 6082 aluminium alloys with a wall thickness that changed from 4.5 mm to 2.0 mm at different positions in the tube. Their work extruded tubes at two ram speeds (0.8 mm/s and 3.3 mm/s and two temperatures 400°C and 500°C). They used EBSD to investigate the misorientation angles of the grain and sub-grain boundaries in order to investigate the influence of alloy composition, temperature and strain (extrusion ratio). They determined that a fibrous grain texture was predominant in the 6082 alloy in all cases except at the higher ram speed of 3.3 mm/s and the higher extrusion temperature of 500°C where fully recrystallized elongated grains were observed. In contrast, for the 6060 alloy a fibrous textured structure developed only at the lower ram speed of 0.8 mm/s and the lower extrusion temperature of 400°C. They attributed this observation to the high manganese content in the 6082 alloy acting as a recrystallisation inhibitor. They also noted that the fibrous microstructures were characterized by elongated grains with high angle grain boundaries (HAGBs > 15°) and both low angle boundaries (LABs < 5°) as well as medium angle boundaries (MABs between 5° - 15°) embedded in the grains.

In the present work on FSW of seamless tubes of 6082 alloy, sample preparation for EBSD involved initial metallographic grinding, followed by mechanical polishing with 0.25 µm diamond suspension and a final polish using 0.05 µm colloidal silica suspension. The final step involved electro-etching the surface using Barkers reagent (a solution of 4 ml fluoroboric acid in 200 ml water), at a voltage of 20 V for 110 sec. EBSD analysis was performed with a JOEL JSM-7001F SEM equipped with an Oxford Instruments EBSD detector. An accelerating voltage of 15 kV was used to scan the sample, and the step size and scan area size were adapted to the size of the microstructural features under examination in order to optimise use of the instrument time. Figure 12 shows the welded specimen and identifies the five regions chosen for EBSD analysis, namely A and E in the as-extruded tube, B in the TMAZ on the advancing side (AS) of the weld D in the TMAZ of the retreating side (RS) and C in the stir zone (SZ) of the weld. Table 5 gives details of the dimensions and step size of the 5 regions selected for EBSD analysis.

A significant amount of microstructural information can be accessed using EBSD techniques, as outlined by Maitland and Sitzman (2007), including 2D maps showing the basic size and shape of the grains. In addition, however, because the phase and orientation at each pixel in the map is also known, EBSD data processing software can generate a variety of additional visual and analytical information, including overall preferred orientation (texture), prevalence and distribution of grains in specific orientations, phase distribution, state of strain and local variations in residual strain, and character and distribution of grain boundaries. Figure 13 gives the Euler angle orientation map for region B in the welded sample that is particularly revealing, because it extends across from the as-extruded tube, through the TMAZ and into the SZ. In general, similar colours[1] indicate similar grain orientations, so the image provides a display of general microstructure, since the basic grain structure and a general idea of strength of texture may be discerned at a glance. However, it is not intuitive to understand the relationship between specific colours and their corresponding orientations, so inverse pole figures are often used to display EBSD data.

The interest in this work primarily centres on texture and on grain boundary misorientation, and Figure 14a shows information on the distribution of HAGBs (> 15°) and LABs (< 15°) in the extruded tube, while Figure 14b shows recrystallisation data constructed from consideration of the average sub-grain misorientation. In the SZ, the number of high angle boundaries decreases (Figure 15a) and the number of fine recrystallized grains increases, as would be expected, in a region that has undergone dynamic recrystallisation (Figure 15b). Figure 16 shows the relevant average pole and inverse pole orientation figures for the as-extruded tube and Figure 17 gives the same data for the SZ. The grain size has undergone a very significant refinement in the SZ as revealed by the EBSD data for average grain size expressed as the diameter of a circle of equivalent area; this is 14.9 μm with an aspect ratio of 4.4 in the extruded tube and 3.1 μm with an aspect ratio of 2.0 in the SZ. Figures 16 and 17 indicate that a significant degree of texture is present in both the extruded tube and in the SZ, which is in agreement with the observations made by Negendank et al. (2016) regarding extruded tubes of 6082 and by Wang et al. (2016) on the SZ in 6082 alloy. The degree of texture is higher in the SZ and, in agreement with the results of Negendank et al. (2016) the textured microstructure of the extruded tube considered in the present work is characterised by elongated grains with high angle grain boundaries and low angles boundaries embedded in the grains. The texture in the centre of the SZ is predominantly of the form [1 0 1] parallel with the X0 projection direction with a secondary amount of the form [0 0 1] parallel with the Z0 projection direction, which is agreement with the component C shear texture found by Wang et al. (2016) in the middle of the SZ of their 6082 alloy.

[1] Coloured images are available in the on-line version of the paper.

Figure 18 shows the Y0 inverse pole figure (IPF) for region B of the weld. The grain colour in the IPF map indicates the plane within the grain that is orientated normal to the Y0 viewing direction of the specimen. For cubic phases, full red, green, and blue are assigned to grains whose <100>, <110> or <111> axes, respectively, are parallel with the projection direction of the IPF (in this case, the surface-normal in the Y0 direction). Intermediate orientations are coloured by an RGB mixture of the primary components. This image can be compared with the Euler angle orientation map of the same region shown in Figure 13; recalling that the value of each Euler angle is individually set to a colour scale (normally red, green, and blue for Euler angles φ_1, Φ, and φ_2, respectively), and the three are combined into a single RGB colour, similar colours therefore indicating similar absolute orientations. In the case of the IPF colour map in Figure 18, it clearly shows that a significant reorientation of grains occurs in the TMAZ with many of the grains having their <110> directions orientated parallel with the Y0 surface normal.

Conclusions

The paper has presented details of the development of a friction stir welding process for joining small diameter 6082 aluminium alloy tubes. To the author's knowledge, this is one of the first such developments to be reported in the FSW literature and as such, full details of the process development have been provided. The weld zone microstructure has been described using EBSD techniques and the tensile properties of the welds have been determined using both complete welded tube specimens and microtensile specimens cut from the tubes. The following conclusions can be drawn from this work:

1. A viable FSW technique has been developed for nominal 38 mm OD 6082 aluminium alloy tube with a 3.0 mm wall thickness. The process uses a tool with a retractable pin and is capable of producing small-scale production runs (circa 100) of welded tube specimens with consistent tensile and fatigue properties.

2. Microstructural analysis of the weld zone using EBSD techniques has shown that the extruded tube has a textured microstructure that is characterised by elongated grains with high angle grain boundaries and low angle boundaries embedded in the grains, in agreement with results reported by Negendank et al. (2016) for 32 mm square extruded 6082 tube with similar wall thickness of 2 mm or 4.5 mm.

3. The central region of the stir zone in the weld shows a very strong shear texture of the form [1 0 1] parallel with the X0 projection direction with a secondary amount of the form [0 0 1] parallel with the Z0 projection direction which is agreement with the component C shear texture found by Wang et al. (2016) in the middle of the SZ of their 6082 alloy.

4. The tensile strength of the extruded 6082-T6 tube is 303 MPa and the joint efficiency of the weld was 0.55 for both complete tube specimens and microtensile specimens. This

compares well with values reported in the literature for 6082 alloy and flat plate specimens 3 mm thick by (Moreira et al., 2009).

Acknowledgements

This work has been supported by the Leverhulme Trust through an International Network grant IN-2012-107 and their support is gratefully acknowledged.

References

American Welding Society, A.N.S.I., 2010. AWS D17.3/D17.3M:2010 Specification for friction stir welding of aluminum alloys for aerospace hardware, Miami, FL.

Borrego, L.P., Abreu, L.M., Costa, J.M., GFerreira, J.M., 2003. Aanalysis of low cycle fatigue in AlMgSi aluminium alloys. Anales de Mecanica de la Fractura 20, 179-184.

Burford, D., Widener, C., Tweedy, B., 2006. Advances in friction stir welding for aerospace applications, 6th AIAA Aviation Technology, Integration and Operations Conference. American Institute of Aeronautics and Astronautics, Wichita, Kansas.

Chen, B., Chen, K., Hao, W., Liang, Z., Yao, J., Zhang, L., Shan, A., 2015. Friction stir welding of small-dimension Al3003 and pure Cu pipes. Journal of Materials Processing Technology 223, 48-57.

Cho, J.-H., Kim, W.J., Lee, C.G., 2014. Evolution of Microstructure and Mechanical Properties During Friction Stir Welding of A5083 and A6082. Procedia Engineering 81, 2080-2085.

Colligan, K.J., 2004. Friction stir welding for ship construction, Harrisburg, PA, p. 6.

Dickerson, T.L., Przydatek, J., 2003. Fatigue of friction stir welds in aluminium alloys that contain root flaws. International Journal of Fatigue 25, 1399-1409.

Doos, Q.M., Abdul wahab, B., 2012. Experimental study of friction stir welding of 6061-t6 aluminum pipe. International Journal of Mechanical Engineering and Robotics Research 1, 143-156.

James, M.N., Bradley, G.R., Lombard, H., Hattingh, D.G., 2005. The relationship between process mechanisms and crack paths in friction stir welded 5083-H321 and 5383-H321 aluminium alloys. Fatigue & Fracture of Engineering Materials & Structures 28, 245-256.

James, M.N., Hughes, D.J., Hattingh, D.G., Bradley, G.R., Mills, G., Webster, P.J., 2004. Synchrotron diffraction measurement of residual stresses in friction stir welded 5383-H321 aluminium butt joints and their modification by fatigue cycling. Fatigue & Fracture of Engineering Materials & Structures 27, 187-202.

Kamp, N., Sullivan, A., Robson, J.D., 2007. Modelling of friction stir welding of 7xxx aluminium alloys. Materials Science and Engineering: A 466, 246-255.

Lammlein, D.H., Gibson, B.T., DeLapp, D.R., Cox, C., Strauss, A.M., Cook, G.E., 2012. The friction stir welding of small-diameter pipe: an experimental and numerical proof of concept for automation and manufacturing. Proceedings of the Institution of Mechanical Engineers, Part B: Journal of Engineering Manufacture 226, 383-398.

Maitland, T., Sitzman, S., 2007. Electron Backscatter Diffraction (EBSD) Technique and Materials Characterization Examples, In: Zhou, W., Wang, Z.L. (Eds.), Scanning Microscopy for Nanotechnology: Techniques and Applications. Springer New York, New York, NY, pp. 41-75.

Moreira, P.M.G.P., Santos, T., Tavares, S.M.O., Richter-Trummer, V., Vilaça, P., de Castro, P.M.S.T., 2009. Mechanical and metallurgical characterization of friction stir welding joints of AA6061-T6 with AA6082-T6. Materials & Design 30, 180-187.

NASA, 2012. EM30 MSFC Technical Standard 3679: Process Specification – Welding Aerospace Hardware, Alabama.

Negendank, M., Taparli, U.A., Gall, S., Müller, S., Reimers, W., 2016. Microstructural evolution of indirectly extruded seamless 6xxx aluminum tubes with axial variable wall thickness. Journal of Materials Processing Technology 230, 187-197.

Peterson, J., Hall, J., Steel, R.J., Babb, J., Collier, M., Packer, S.M., 2011. Out of position friction stir welding of casing and small diameter tubing or pipe, In: Office, U.S.P.a.T. (Ed.), USA.

Shah, S., Tosunoglu, S., 2012. Friction stir welding: current state of the art and future prospects, 16th World Multi-Conference on Systemics, Cybernetics and Informatics, Orlando, Florida, p. 6.

Steel, R.J., Packer, S.M., Fleck, R.D., Sanderson, S., Tucker, C., 2013. Advances in FSW and new applications A2 - Fujii, Hidetoshi, Proceedings of the 1st International Joint Symposium on Joining and Welding. Woodhead Publishing, pp. 125-127.
Thomas, W.M., Nicholas, E.D., 1997. Friction stir welding for the transportation industries. Materials & Design 18, 269-273.
Wang, T., Zou, Y., Matsuda, K., 2016. Micro-structure and micro-textural studies of friction stir welded AA6061-T6 subjected to different rotation speeds. Materials & Design 90, 13-21.
Wu, A.P., Song, Z.H., Nakata, K., Liao, J.S., 2013. Defects and the properties of the dissimilar materials FSW joints of titanium alloy TC4 with aluminum alloy 6061 A2 - Fujii, Hidetoshi, Proceedings of the 1st International Joint Symposium on Joining and Welding. Woodhead Publishing, pp. 243-248.

Table 1 Weld process parameters used to make the trial welds shown in Figure 4.

Weld	Feed Rate (mm/min)	Tool rpm	Plunge Depth (mm)	Pin Length (mm)	Tool Tilt Angle	Total Rotational Angle
1	100	600	2.40	2.30	2°	360°
4	100	800	2.40	2.35	2.5°	360°
3	100	800	2.40	2.35	2.5°	720°
2	50	800	2.45	2.35	2.5°	720°

Table 2 Tensile and torsional strength data for the welded 6082-T6 tubes. Superscript 1 indicates microtensile data and superscript 2 relates to complete tube tests.

Parent plate[1]	Tension	303 MPa
Weld zone[1]	Tension	169 MPa
Weld zone[2]	Tension	168 MPa
Weld zone[2]	Torsion	118 MPa

Table 3 Chemical composition of the 6082-T6 aluminium tubes.

	Mg	Si	Mn	Fe	Zn	Cu	Ti	Cr	Al
Specification	0.60-1.20	0.70-1.30	0.40-1.00	0.50	0.20	0.10	0.10	0.25	Balance
Tubes	0.647	0.988	0.526	0.222	0.021	0.034	0.012	0.006	Balance

Table 4 Parent plate grain size and aspect ratio in the L-T, L-S and T-S metallographic planes.

Plane	Grain dimension (μm)			Aspect Ratio
	L-direction	T-direction	S-direction	
L-T	4.3	4.7	-	1.09
L-S	5.2	-	3.7	1.41
T-S	-	5.1	4.0	1.28

Table 5 Dimensions and step size of the 5 regions selected for EBSD analysis.

Scan region	Scan Size (μm)	Step Size (μm)	Scale Bar (μm)
A	409 x 250	0.5	100
B	680 x 250	0.3	200
C	250 x 250	0.2	100
D	680 x 250	0.3	200
E	409 x 250	0.5	100

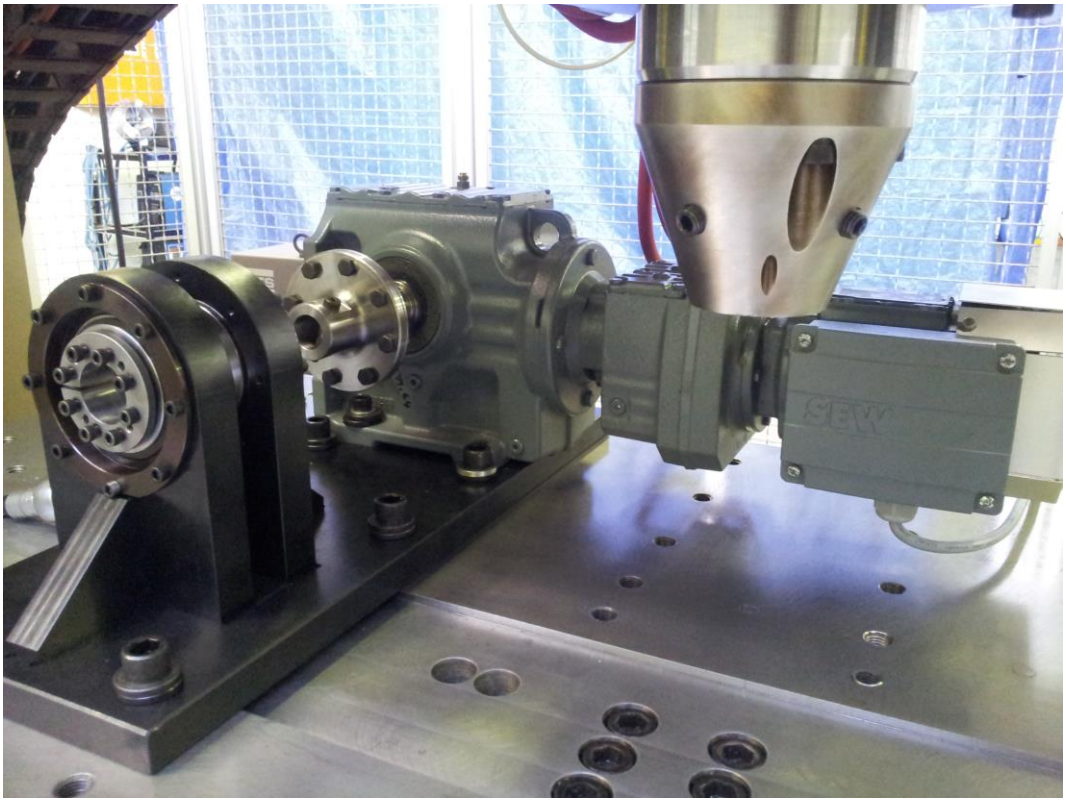

Figure 1 The various tube welding system components mounted on the table of the I-STIR platform.

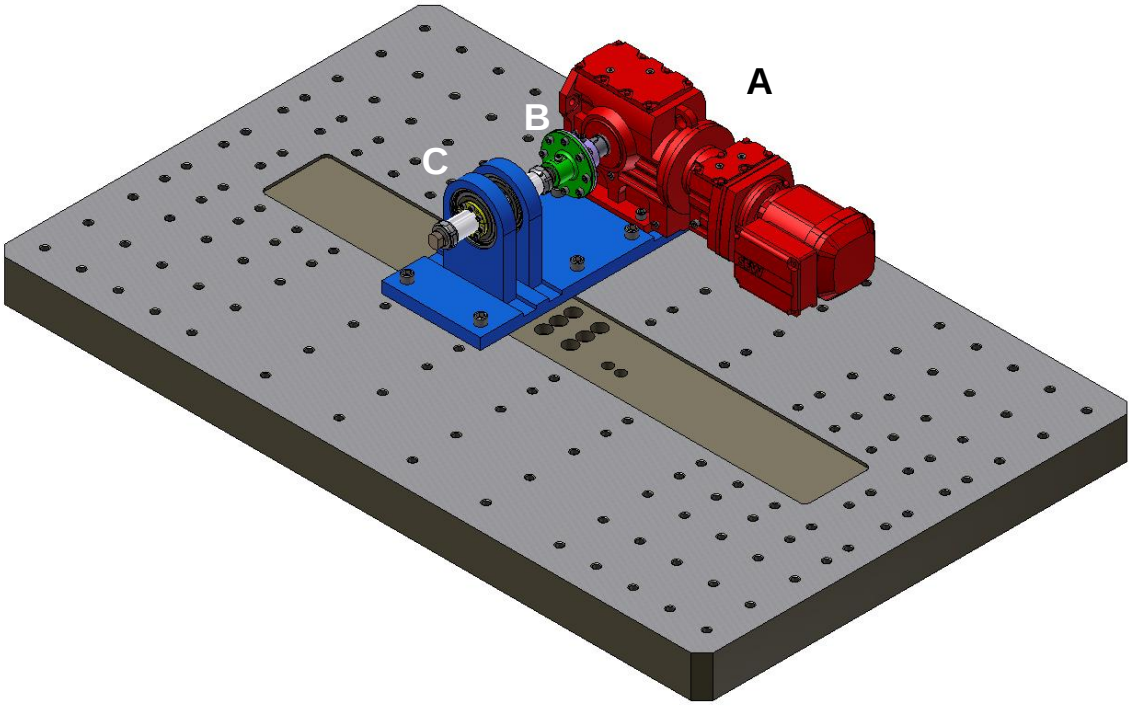

Figure 2 Schematic diagram showing the tube rotation drive and the clamping system mounted on the bed of the I-STIR FSW platform. The three main components A, B, and C are described in the paper.

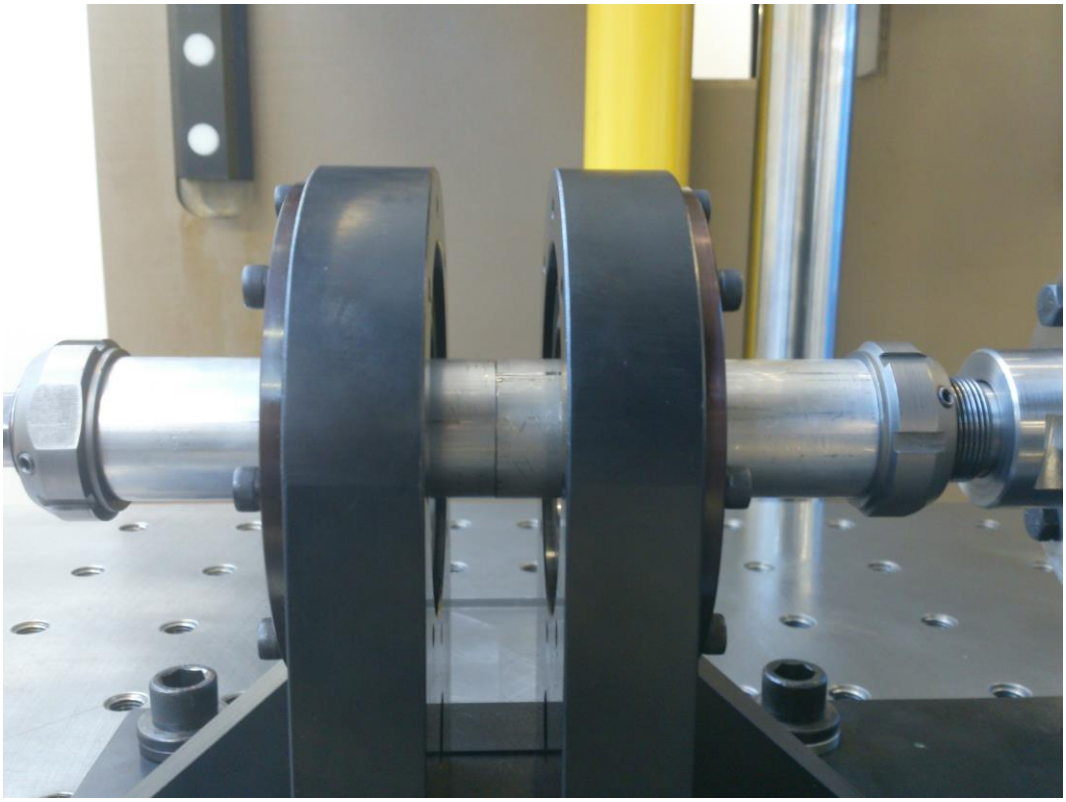

Figure 3a Two sections of tube ready for welding in the clamping system.

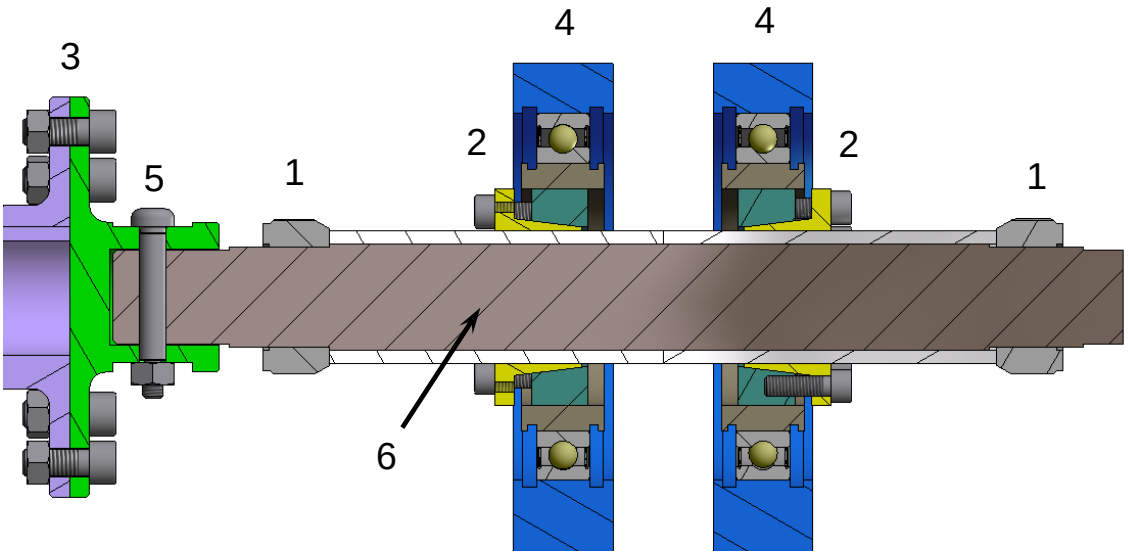

Figure 3b Sectioned view of the various components in the support and clamping system; the internal mandrel is clearly shown here. The various components are numbered and described in the paper.

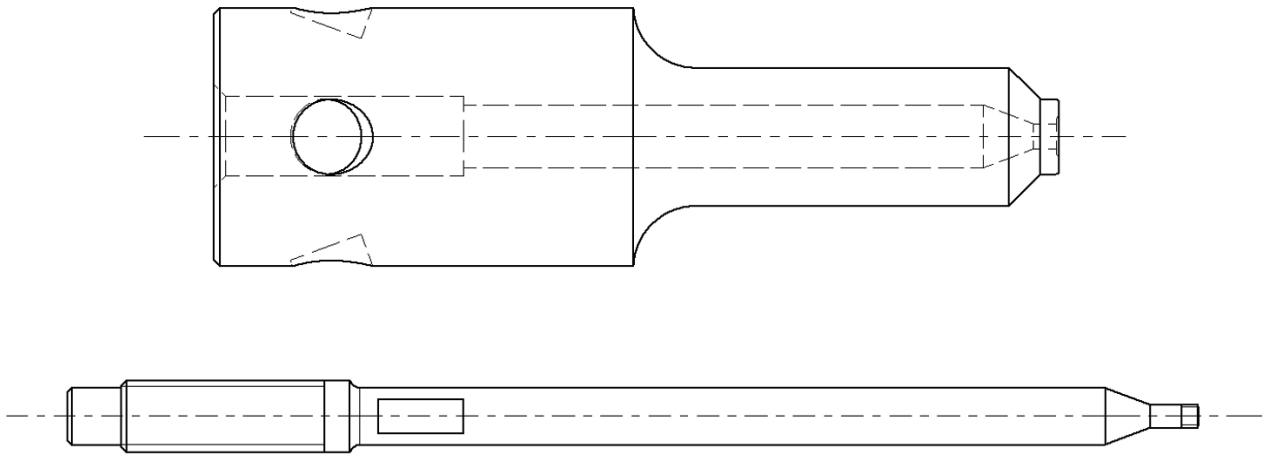

Figure 4 Schematic illustration of the tool shoulder (top) and the pin (bottom). The shoulder is 135 mm long while the overall length of the pin is 200 mm.

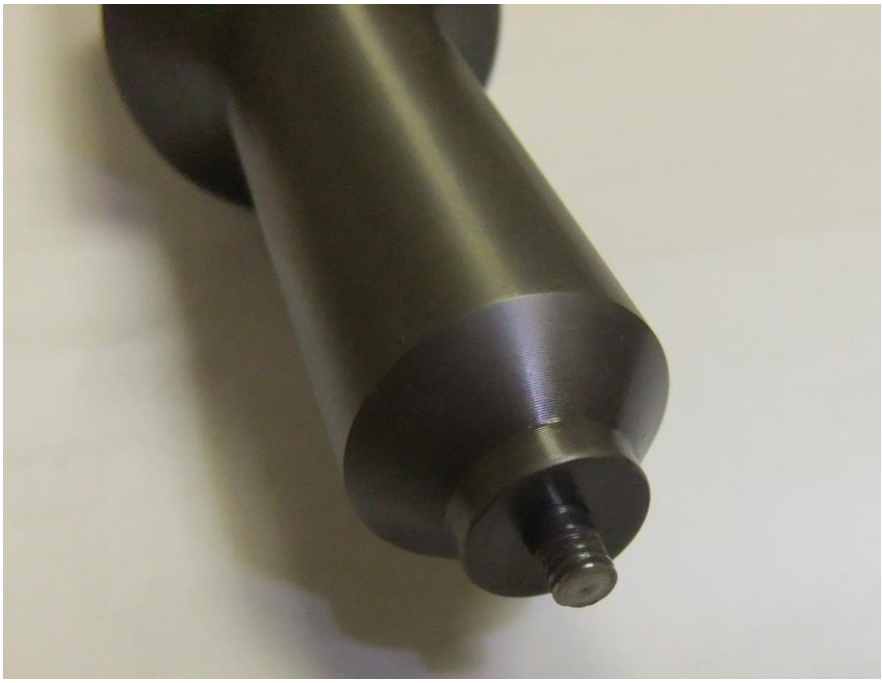

Figure 5 Assembled tool shoulder and pin heat treated to give a hardness of Rockwell C 54.

Figure 6 Illustration of the HMI for the automatic control mode. The various input data are described in the paper.

Figure 7 Illustration of the influence on weld surface finish of spindle rotational speed, tool feed rate and number of revolutions of shoulder contact. The parameters corresponding with the welds numbered 1 to 4 are given in Table 1.

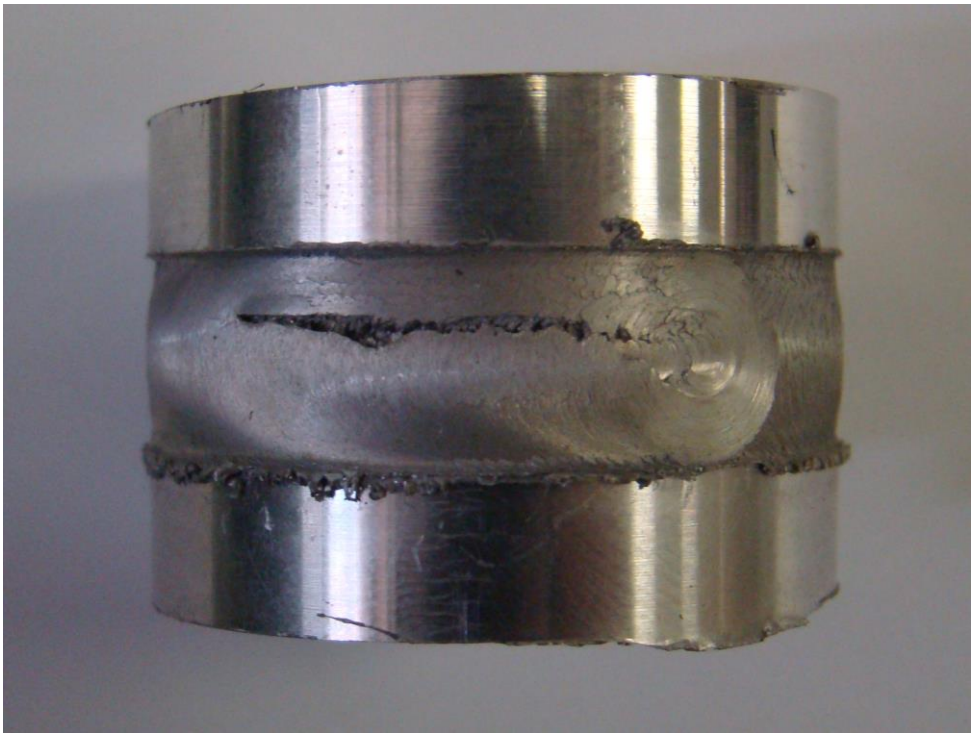

Figure 8 Illustration of the type of weld defect that can occur when the tool pin is misaligned with the centre of the joint and/or tube ovality or eccentricity problems exist, even when the process parameters are appropriate.

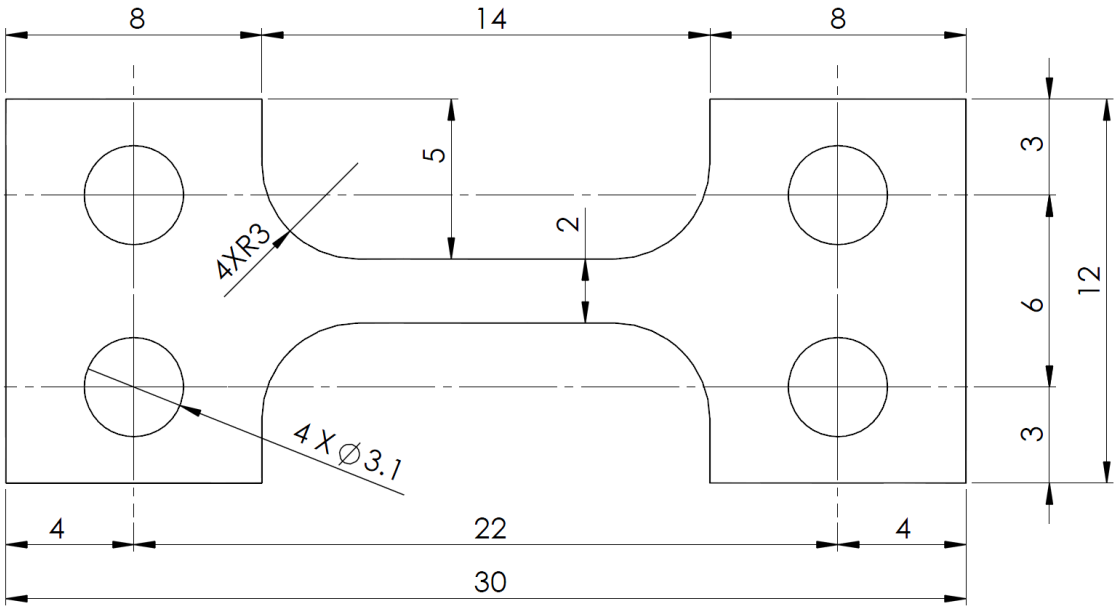

Figure 9 Microtensile specimen dimensions in millimetres. The specimen has a curvature due to the tube of approximately 15.7 mm and requires special gripping arrangements to test.

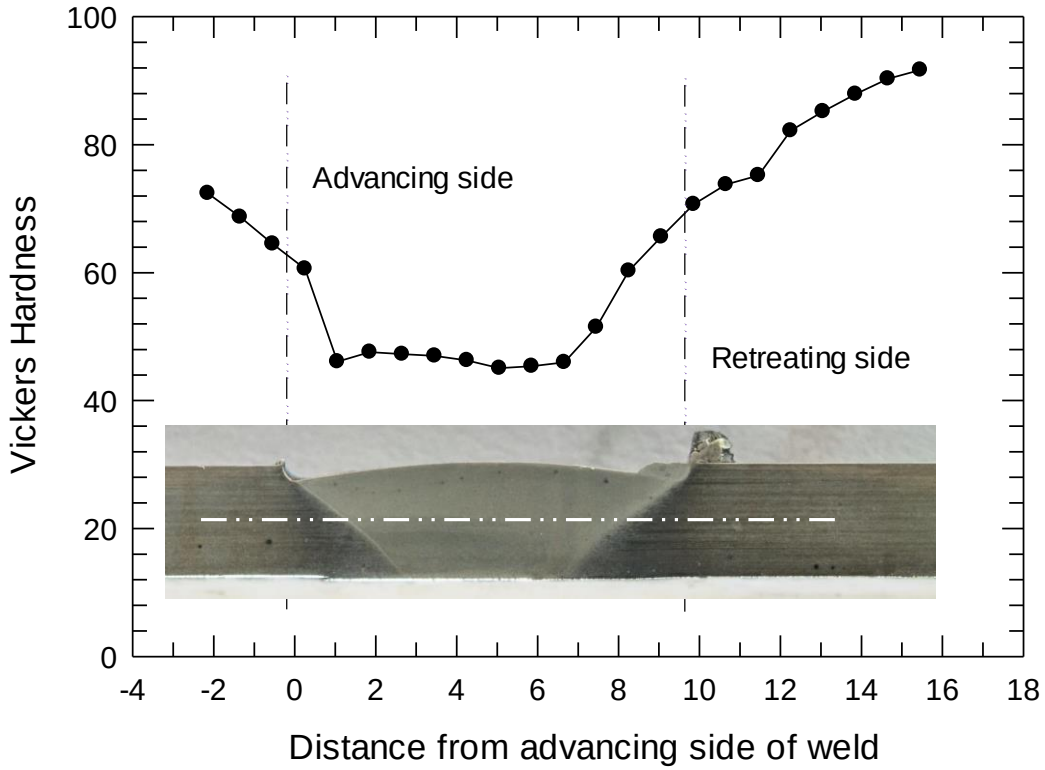

Figure 10 Vickers hardness variation measured across the weld zone at the mid-depth (marked with the white dashed line) of the tube using a 500gf load. The weld cross-section is also shown in the figure at the same scale.

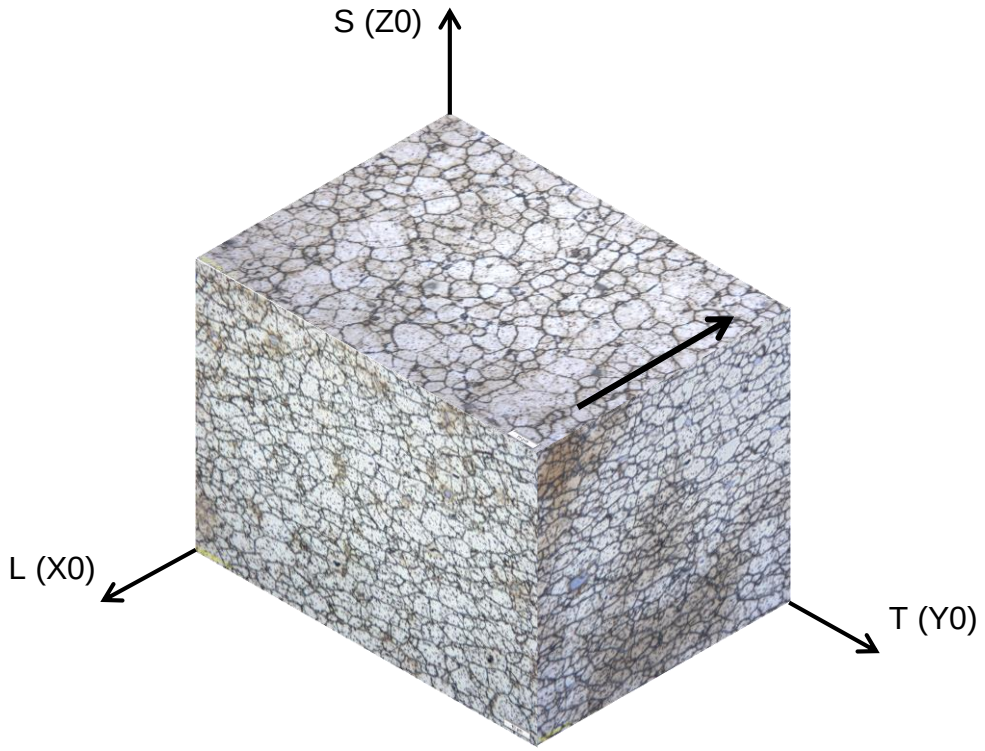

Figure 11 3D representation of the microstructure of the 6082-T6 aluminium alloy tube, etched in Weck's solution. The arrow marks the extrusion direction and X0, Y0 and Z0 axes are also shown to allow a cross-correlation with the EBSD images.

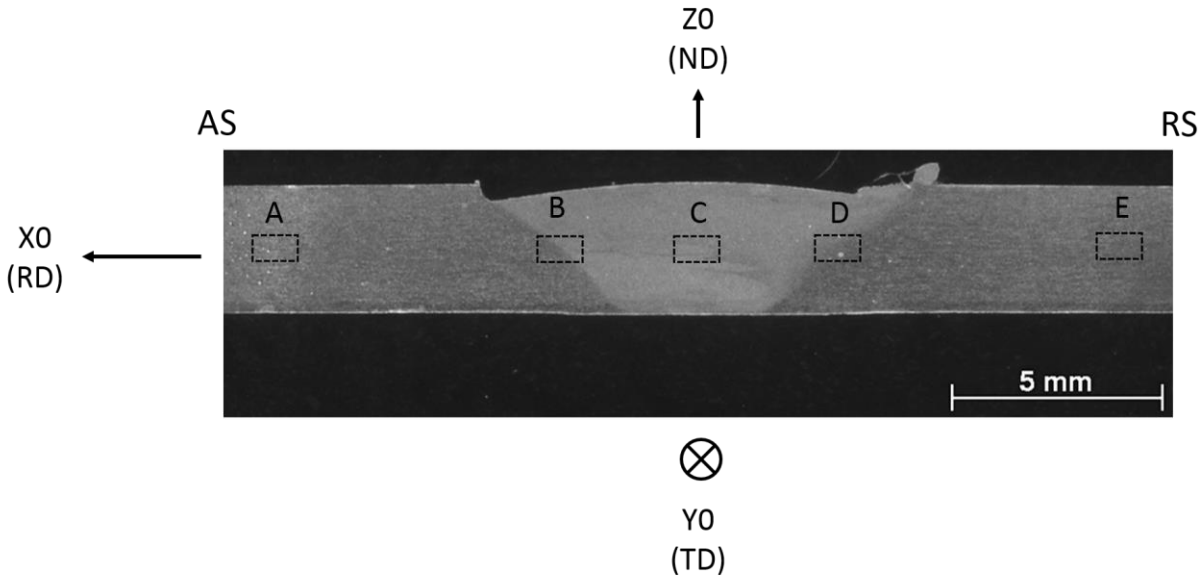

Figure 12 Welded specimen used for the EBSD analysis showing the five regions analysed and also showing the axis convention used, where X0 is the extrusion direction along the tube, Y0 is in the circumferential direction (coinciding with the welding direction) and Z0 is the direction normal to the surface of the tube. AS refers to the advancing side of the weld and RS to the retreating side.

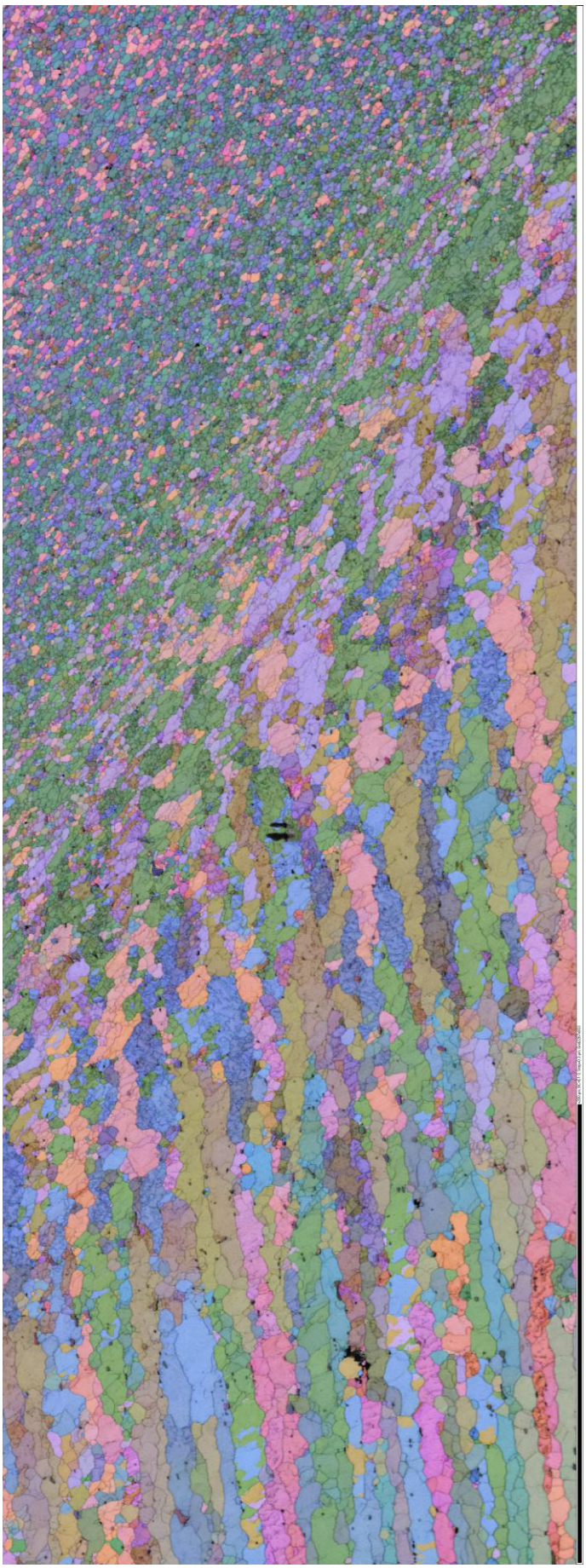

Figure 13 Euler angle orientation map of region B in the welded specimen. This region extends across from the as-extruded tube, through the TMAZ and into the SZ. The black line indicates 200 μm here.

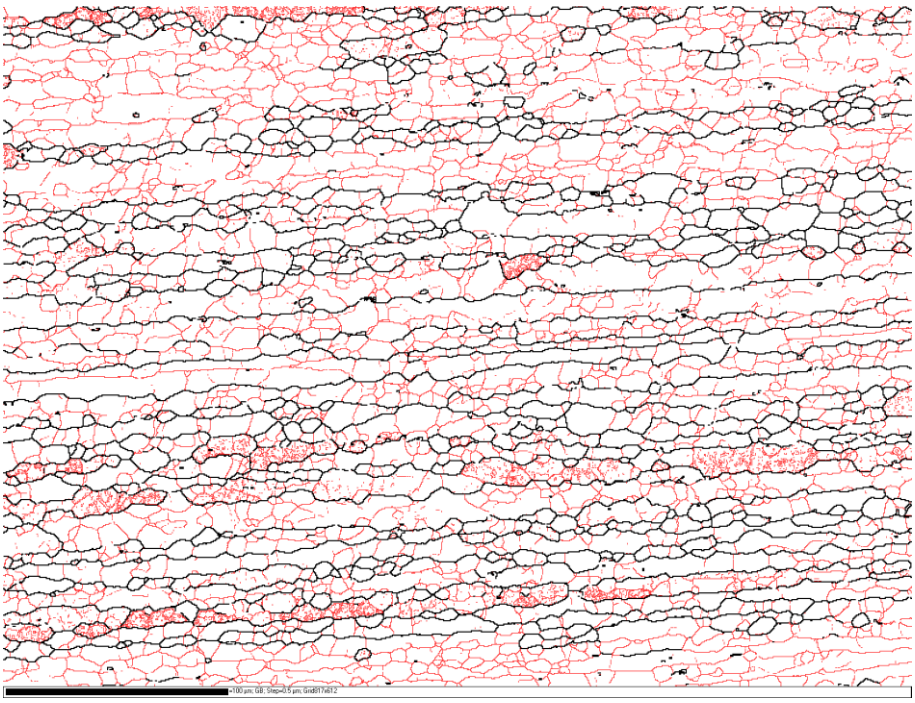

Figure 14a Image showing the density and distribution of LABs (red) and HAGBs (black) in region A of the welded sample. The black line on the bottom left of the image indicates 100 µm.

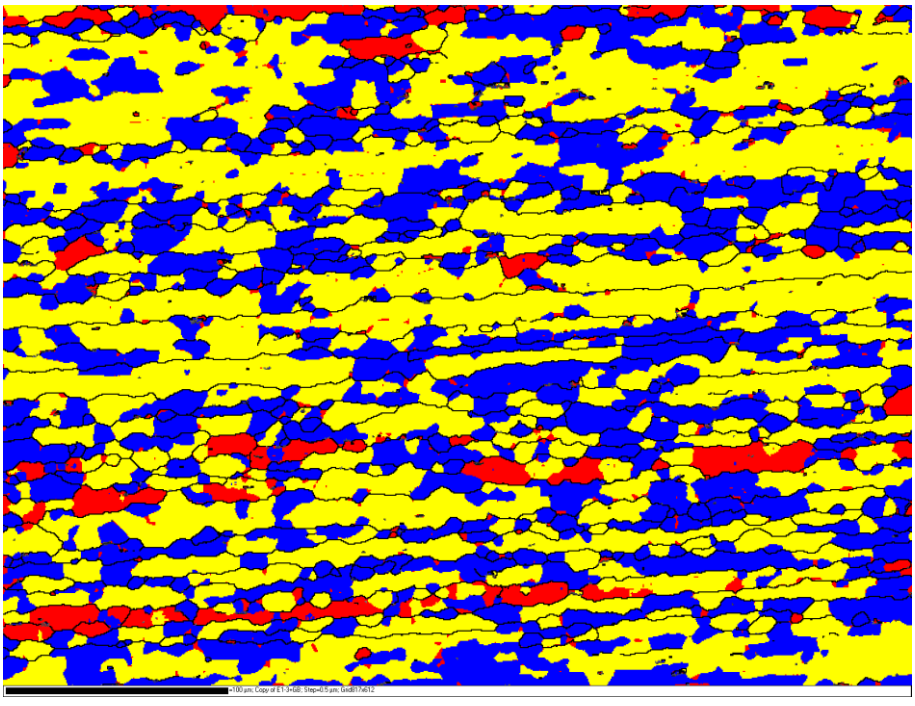

Figure 14b Image of the same area in region A, showing the recrystallised fraction defined from the average sub-grain misorientation; blue grains are either recrystallized or have low sub-grain misorientation (< 1°), yellow indicates marginally strained grains (1° < misorientation < 7.5°) and red shows highly strained grains (> 7.5°).

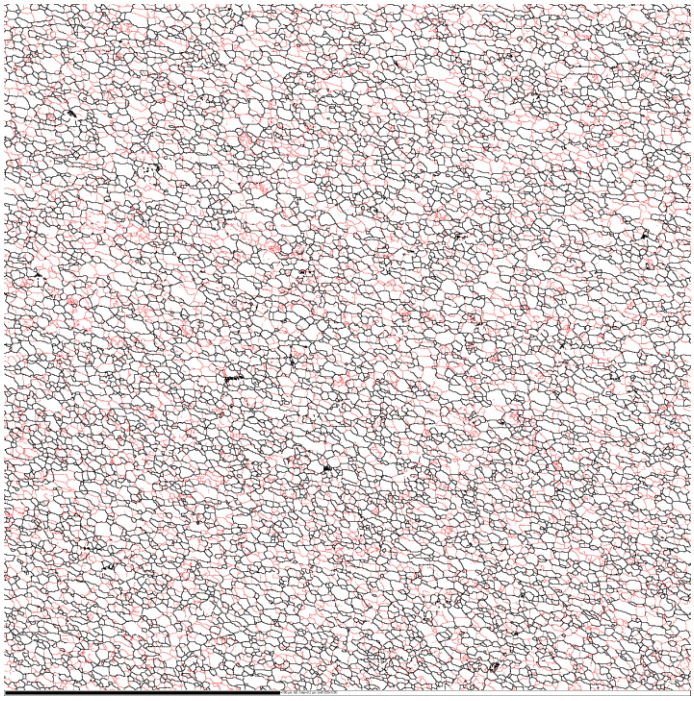

Figure 15a Image showing the density and distribution of LABs (red) and HAGBs (black) in region C of the welded sample. The black line on the bottom left of the image indicates 100 µm.

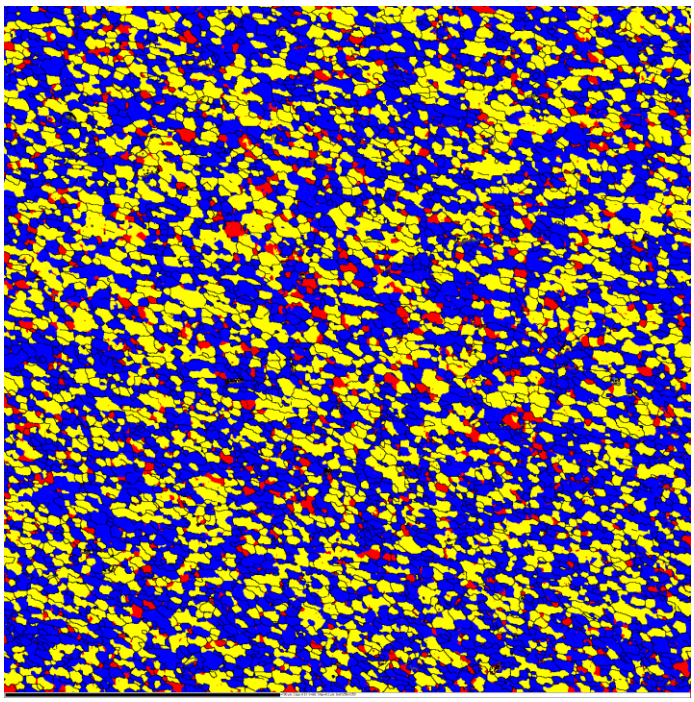

Figure 15b Image of the same area in region C, showing the recrystallised fraction defined from the average sub-grain misorientation.

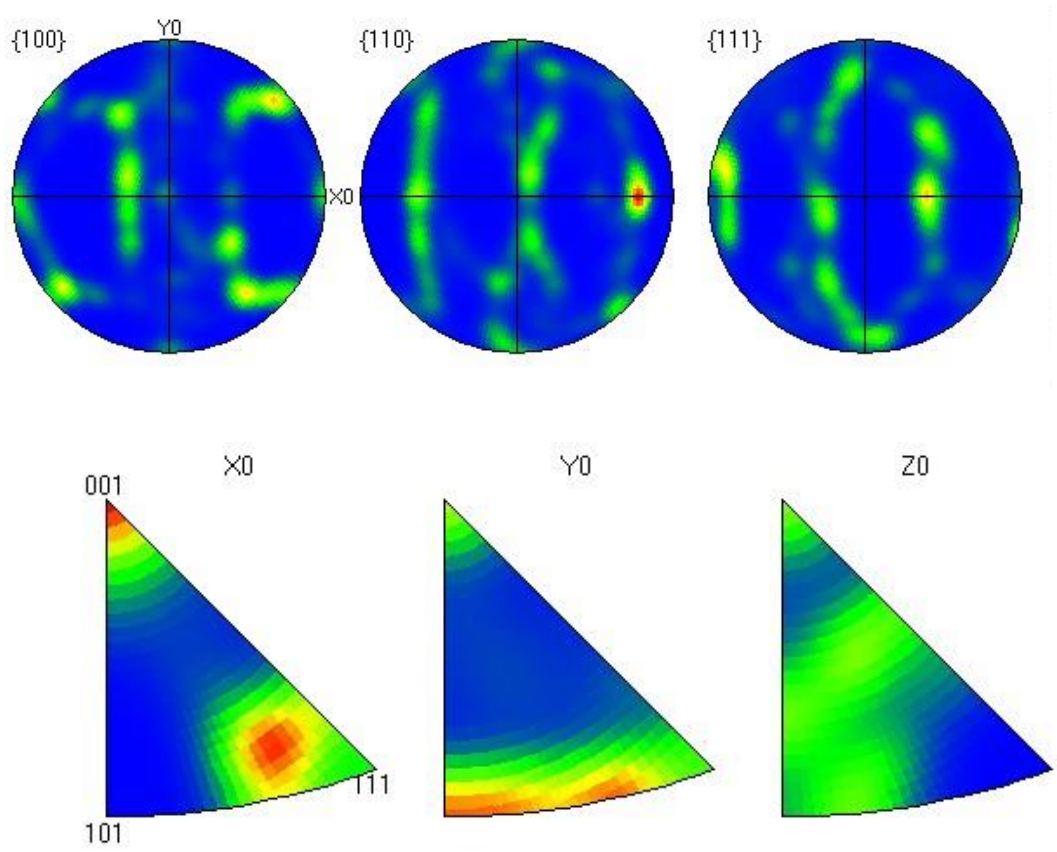

Figure 16 Region A, i.e. the as-extruded tube alloy: Top (circles) - Pole figures plotting the relative orientation density of the stereographic projections of the {1 0 0}, {1 1 0} and {1 1 1} planes with respect to the X0-Y0 plane, i.e. normal to the Z0 direction.
Bottom (triangles) - Inverse pole figures indicating the relative density and orientation of the grains whose <001>, <101> or <111> axes are parallel to the projection direction of the inverse pole figure, i.e. X0, Y0 and Z0.

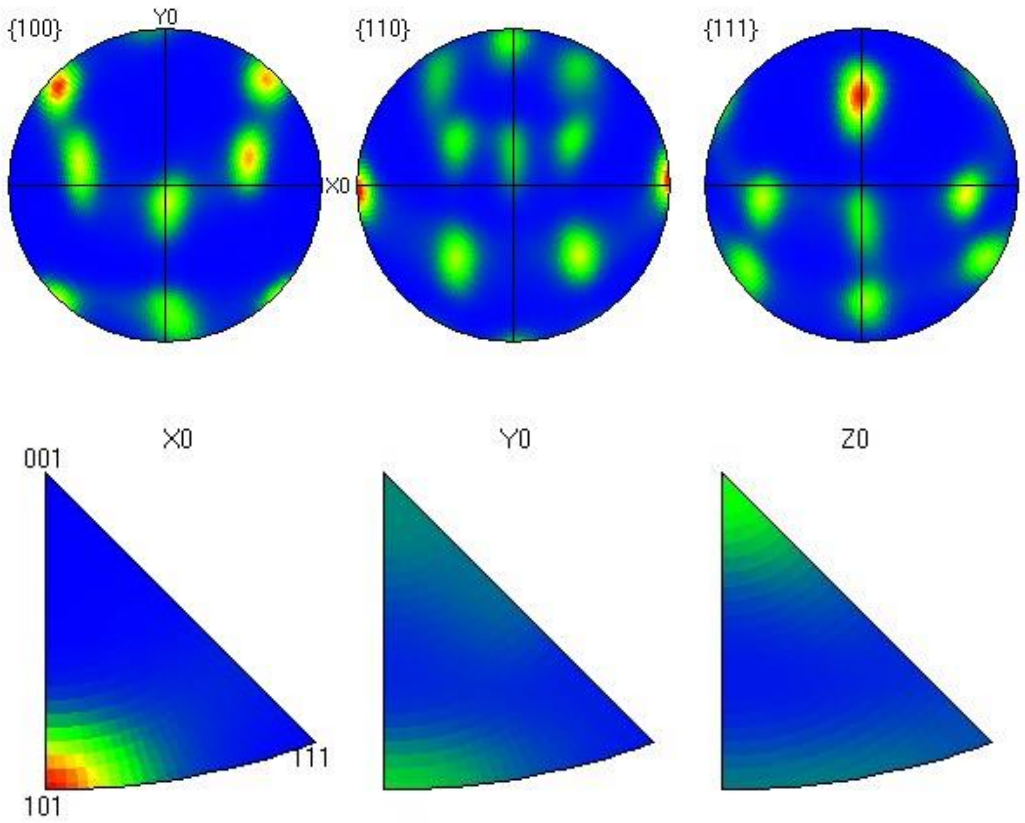

Figure 17 Pole and inverse pole figures for region C in the welded specimen, i.e. the SZ.

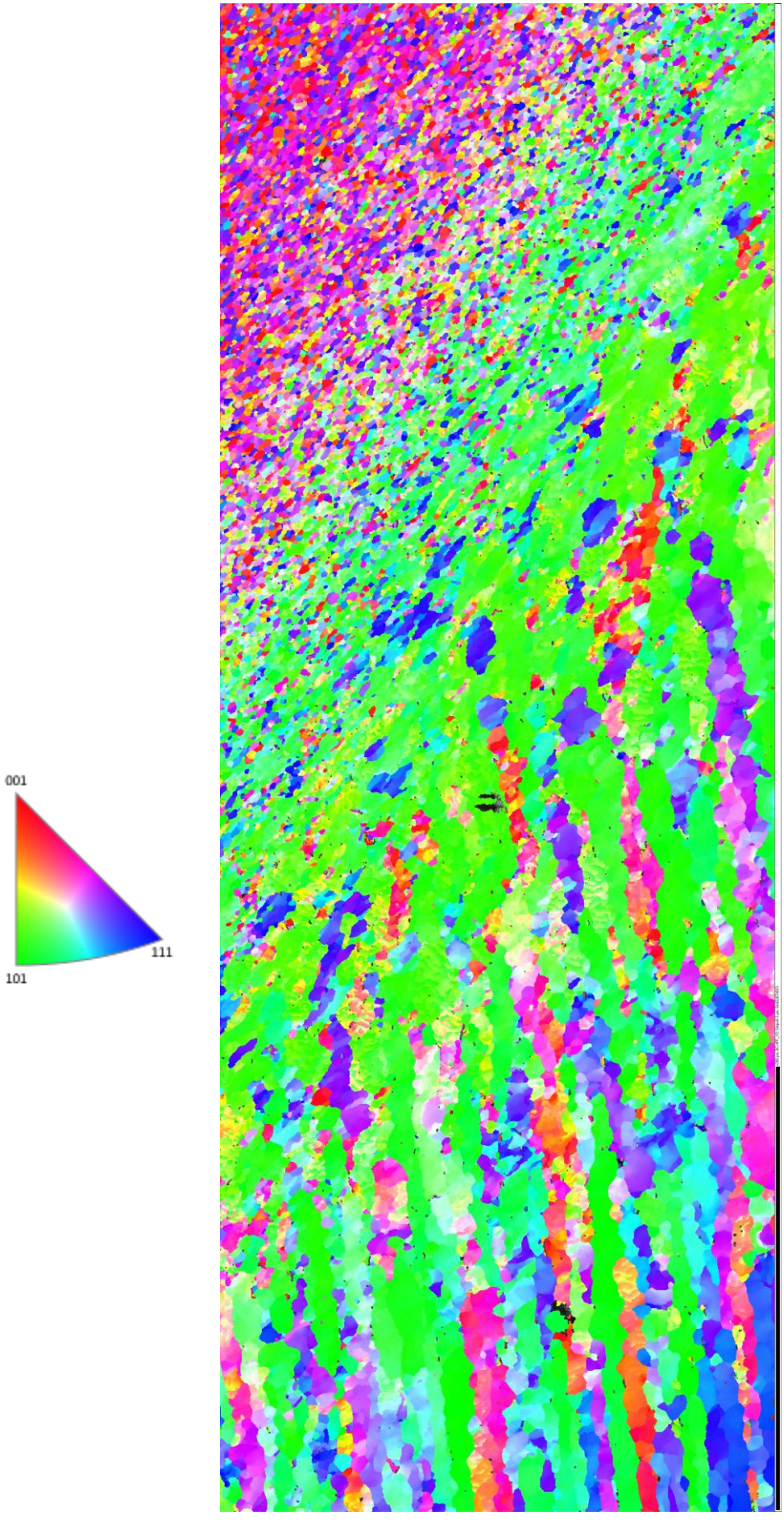

Figure 18 Inverse pole figure for region B in the welded specimen. Grains are coloured in accordance with the standard stereographic triangle for the cubic system (inset image).